



Deposited via The University of Sheffield.

White Rose Research Online URL for this paper:

<https://eprints.whiterose.ac.uk/id/eprint/128928/>

Version: Published Version

Article:

Joseph, K., Stennett, M.C., Hyatt, N.C. et al. (2017) Iron phosphate glasses: Bulk properties and atomic scale structure. *Journal of Nuclear Materials*, 494. pp. 342-353. ISSN: 0022-3115

<https://doi.org/10.1016/j.jnucmat.2017.07.015>

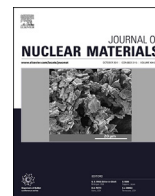
Reuse

This article is distributed under the terms of the Creative Commons Attribution (CC BY) licence. This licence allows you to distribute, remix, tweak, and build upon the work, even commercially, as long as you credit the authors for the original work. More information and the full terms of the licence here:

<https://creativecommons.org/licenses/>

Takedown

If you consider content in White Rose Research Online to be in breach of UK law, please notify us by emailing eprints@whiterose.ac.uk including the URL of the record and the reason for the withdrawal request.



Iron phosphate glasses: Bulk properties and atomic scale structure



Kitheri Joseph ^{a,*}, Martin C. Stennett ^b, Neil C. Hyatt ^b, R. Asuvathraman ^a, Charu L. Dube ^b, Amy S. Gandy ^b, K.V. Govindan Kutty ^a, Kenny Jolley ^c, P.R. Vasudeva Rao ^a, Roger Smith ^c

^a Chemistry Group, Indira Gandhi Centre for Atomic Research, Kalpakkam 603 102, Tamil Nadu, India

^b Department of Materials Science & Engineering, The University of Sheffield, Mappin Street, Sheffield S1 3JD, UK

^c Department of Mathematical Sciences, Loughborough University, Loughborough LE11 3TU, UK

ARTICLE INFO

Article history:

Received 10 November 2016

Received in revised form

30 June 2017

Accepted 6 July 2017

Available online 8 July 2017

ABSTRACT

Bulk properties such as glass transition temperature, density and thermal expansion of iron phosphate glass compositions, with replacement of Cs by Ba, are investigated as a surrogate for the transmutation of ¹³⁷Cs to ¹³⁷Ba, relevant to the immobilisation of Cs in glass. These studies are required to establish the appropriate incorporation rate of ¹³⁷Cs in iron phosphate glass. Density and glass transition temperature increases with the addition of BaO indicating the shrinkage and reticulation of the iron phosphate glass network. The average thermal expansion coefficient reduces from $19.8 \times 10^{-6} \text{ K}^{-1}$ to $13.4 \times 10^{-6} \text{ K}^{-1}$, when 25 wt. % of Cs₂O was replaced by 25 wt. % of BaO in caesium loaded iron phosphate glass. In addition to the above bulk properties, the role of Ba as a network modifier in the structure of iron phosphate glass is examined using various spectroscopic techniques. The Fe^{II} content and average coordination number of iron in the glass network was estimated using Mössbauer spectroscopy. The Fe^{II} content in the un-doped iron phosphate glass and barium doped iron phosphate glasses was 20, 21 and $22 \pm 1\%$ respectively and the average Fe coordination varied from 5.3 ± 0.2 to 5.7 ± 0.2 with increasing Ba content. The atomic scale structure was further probed by Fe K-edge X-ray absorption spectroscopy. The average coordination number provided by extended X-ray absorption fine structure spectroscopy and X-ray absorption near edge structure was in good agreement with that given by the Mössbauer data.

© 2017 The Authors. Published by Elsevier B.V. This is an open access article under the CC BY license (<http://creativecommons.org/licenses/by/4.0/>).

1. Introduction

Iron phosphate glasses are of interest for application in the field of radioactive waste immobilisation due to their high chemical durability [1–6]. Among the various Fe/P atomic ratio, the glass with 40 mol % Fe₂O₃–60 mol % P₂O₅ (IPG) (where the Fe/P atomic ratio = 0.67) is found to be more chemically durable [3]. As indicated by Jantzen [5,6], excellent chemical durability, high solubility for heavy metals, low melting temperatures, rapid melting rates, low corrosion of oxide refractories and inconel alloys and higher (25–50 mass %) waste loading are certain salient features of iron phosphate glass. The glass forming characteristics of iron phosphate glass are demonstrated by immobilizing waste rich in Cs, Mo, U, and Cr [3,7,8] which are poorly soluble in borosilicate glass [9]. In our earlier studies [10], we had demonstrated IPG as a promising matrix for the immobilisation of Cs with respect to higher loading

(50 ± 2 wt. % Cs₂O) and also due to its low (<0.5 wt. %) volatilisation loss during homogenisation of the melt in contrast to ~10 wt. % loss of Cs during immobilisation in borosilicate glass used for clinical applications [11]. Sealed radioactive Cs source is not only used for clinical application, it has other industrial, research and medical applications. Reference [12] contains a good summary of these applications. Because radioactive caesium decays to barium, it is essential to understand the change in the bulk properties (such as density, glass transition temperature, linear thermal expansion) of caesium loaded IPG when the Cs is partly or completely replaced with Ba. In order to understand the effect of complete conversion to Ba loaded iron phosphate glass, the said bulk properties were studied for iron phosphate glass containing 10 and 20 wt. % BaO. As the maximum composition of Cs₂O loaded in IPG was 50 ± 2 wt. % (labelled as IPCs50 henceforth), bulk properties were determined with partial replacement of Cs₂O with 5 wt. % BaO and 25 wt. % BaO. Various other combinations and compositions of Cs/Ba loaded iron phosphate glasses are not part of the present study. A study such as this is essential before immobilizing ¹³⁷Cs in IPG, since ¹³⁷Cs loaded IPG can serve as a γ source for medical application.

* Corresponding author.

E-mail address: joskit@igcar.gov.in (K. Joseph).

2. Experimental

2.1. Glass preparation

Batches of iron phosphate glasses were prepared by mixing various amounts of Cs_2CO_3 (99.9% Aldrich), Fe_2O_3 (99.5%, Fisher Scientific), $\text{NH}_4\text{H}_2\text{PO}_4$ (ADP) (99% Ranbaxy) and $\text{Ba}(\text{OH})_2 \cdot 8\text{H}_2\text{O}$ (99.9% Loba Chemie). The mixture was homogenized by grinding in a mortar and pestle in an inert argon glove box. The mixture was taken in a high density re-crystallized alumina crucible and calcined at 523 K for 1 h prior to melting. Each calcined sample was melted inside an electric furnace in air. The batch composition of each mixture was such that the final amount of glass aimed for was 30 g. The calcined mixture was heated to 1323 K and homogenized for 30 min quenched in air, cooled and weighed. The heating rate was maintained as 10 K min^{-1} . The mixture was re-heated, melted and air quenched by pouring into a graphite mould to get a cylindrical rod of 15 mm height and 10 mm diameter. The remaining molten material was air quenched on a stainless steel plate. The air quenched bulk materials were ball milled and powder samples were used for all the characterization studies except for density measurements. As-quenched granules were used for the density measurements. The percentage weight loss during glass preparation of each glass batch is presented in Table 1. The error in weight measurement was $\pm 0.001 \text{ g}$. A mixture of Fe_2O_3 and $\text{NH}_4\text{H}_2\text{PO}_4$ maintaining a Fe/P atomic ratio of 0.67 was heated in a similar alumina crucible and air quenched at 1423 K for the preparation of un-doped IPG. No measurable corrosion was observed when heated in a high density re-crystallized alumina crucible. The glass inside the alumina crucible could be removed. Fig. 1 shows a photograph of the crucible before and after removal of the IPBa10 glass.

2.2. Characterization

2.2.1. X-ray diffraction

Samples were characterised by XRD (X-ray diffraction) by using a Siemens D500 X-ray diffractometer (equipped with secondary beam curved graphite monochromator) employing $\text{Cu K}\alpha$ radiation. Scans were performed with the step size of 0.05° over a range of $2\theta = 5^\circ\text{--}80^\circ$ with 1 s counting time per step.

2.2.2. Density measurements

The density of each glass was determined by using the Archimedes principle utilising dibutyl phthalate as the liquid medium. Randomly chosen pieces of glasses were subjected to density measurements. The error in the density measurements was $\pm 5 \text{ kg m}^{-3}$.

2.2.3. Differential thermal analysis (DTA)

The DTA was carried out using TG-DTA Setsys Evolution 16/18, M/s. Setaram, France. The instrument was calibrated for temperature as explained previously [10]. A differential thermal analysis was used to determine the glass transition temperature (T_g) of the glasses under present study. The T_g of all the glasses were

determined in flowing argon (rate: 20 ml min^{-1}) using Pt crucibles at a heating rate of 10 K min^{-1} . Blank runs were carried out under similar conditions and the data presented are the blank corrected ones. The glass transition temperature (T_g) is defined as the midpoint temperature of the extensions of the pre and post transition baselines of the DTA curve. The error in the temperature measurement was $\pm 1 \text{ K}$.

2.2.4. Dilatometry

Thermal expansion studies were carried out by means of a home-built push rod dilatometer [14] in air up to 700 K at a heating rate of 2 K min^{-1} using a LVDT (linear variable differential transformer) sensor and quartz push rod. Specimen temperature was measured by a chromel–alumel thermocouple placed very near the specimen. High density thoria pellets were used as standards. The faces of the glass rod (graphite moulded with dimension of 15 mm in height and 10 mm in diameter) were made parallel by polishing with SiC paper (grit 240 and 600). These rods were used for the thermal expansion measurements using the dilatometer. The maximum relative error in the dilatometric measurements was $\pm 2\%$.

2.2.5. Mössbauer spectroscopy

Room temperature ^{57}Fe Mössbauer measurements were carried out using a Wissel spectrometer. Finely powdered specimens were analysed in transmission mode, using a 50 mCi ^{57}Co source embedded in a Rh matrix. Calibration of the data was made relative to $\alpha\text{-Fe}$ and the spectra were measured using a constant acceleration waveform at a velocity range of $\pm 10 \text{ mm s}^{-1}$. Spectral deconvolution was performed using the commercially available software RECOIL [15] by assigning doublets with an extended Voigt-based fitting (xVBF) profile to represent the different Fe oxidation states and coordination environments in the samples. xVBF lineshapes are a convolution of Lorentzian and Gaussian components which represent both the natural lineshape of the emission/absorption process and the site distribution characteristics of amorphous materials [16].

2.2.6. XAS studies

XAS data were acquired on the beam line B18 at Diamond Light Source, Harwell, UK, and beamline X23A2 of the National Synchrotron Light Source, Brookhaven National Laboratory, Upton, NY, USA. Beamline B18 utilises a collimating mirror, a fixed-exit double crystal Si(111) monochromator and a double toroidal focussing mirror. Beamline X23A2 utilises an upwards reflecting, fixed exit, piezo-feedback stabilised Si (311) double crystal monochromator of a Golovchenko-Cowan design, and a single bounce harmonic rejection mirror. Fe K-edge XAS data were acquired on B18 and X23A2 in transmission mode using finely ground specimens dispersed in polyethylene glycol to achieve a thickness of one absorption length. P K-edge XAS data were acquired on B18 in fluorescence mode, under He atmosphere, using finely ground specimens dispersed in a mixture of polyethylene glycol and graphite, oriented at 45° to the incident X-ray beam and detector.

Table 1

Batch composition, observed percentage of weight loss during glass preparation, and the properties measured for the glasses under present study.

Sample	Batch Composition ± 0.5 (wt. %)				% weight loss	Density ± 5 (kg m^{-3})	Molar volume (m^3) $\times 10^5$	Glass transition temperature ± 1 (K)
	Fe_2O_3	P_2O_5	BaO	Cs_2O				
IPBa10	38.6	51.4	10.0	0	0.85	3119	4.79	806
IPBa20	34.3	45.7	20.0	0	0.75	3454	4.34	841
IPCs45Ba5	21.6	28.8	44.6	5.0	1.02	3639	5.19	752
IPCs25Ba25	21.5	28.6	24.9	25.0	0.84	3910	4.36	856

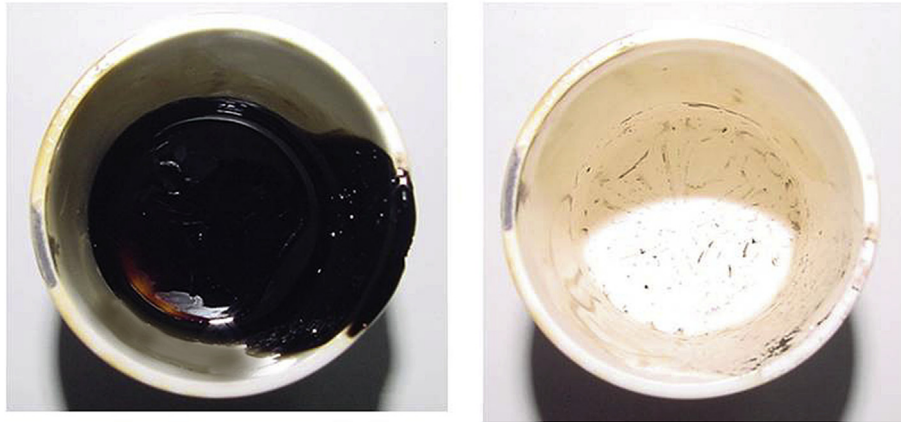


Fig. 1. Photograph showing before and after removal of IPBa10 glass from an alumina crucible.

Incident and transmitted beam intensities were measured using ionization chambers, filled with mixtures of He and Ar or N₂, operated in a stable region of their I/V curve. Fluorescence emission was detected using a four channel Si-drift detector, with appropriate dead time correction as described previously [17]. An iron foil was used as an internal energy calibration where the first inflection point was defined to be 7111.0 eV. Data reduction and analysis was performed using the programmes Athena, Artemis and Hephaestus [18].

3. Results and discussion

3.1. Glass preparation and amorphous nature

The percentage weight loss observed during the preparation of the glasses is shown in Table 1. The weight loss observed was < 1% and thus the batch composition was taken as the glass composition (Table 1). Bulk glass samples were characterised by XRD. The prepared glasses were found to be X-ray amorphous as shown in Fig. 2. The XRD pattern of un-doped IPG [13] is also added in Fig. 2 for comparison. The quenching temperature (Table 1) of either Ba loaded or Ba/Cs loaded IPG was lower than that of un-doped IPG, indicating the effect of addition of modifiers such as Cs₂O or BaO during the synthesis of glass. This is similar to that reported in the literature for Cs loaded IPG [10]. Although the quenching

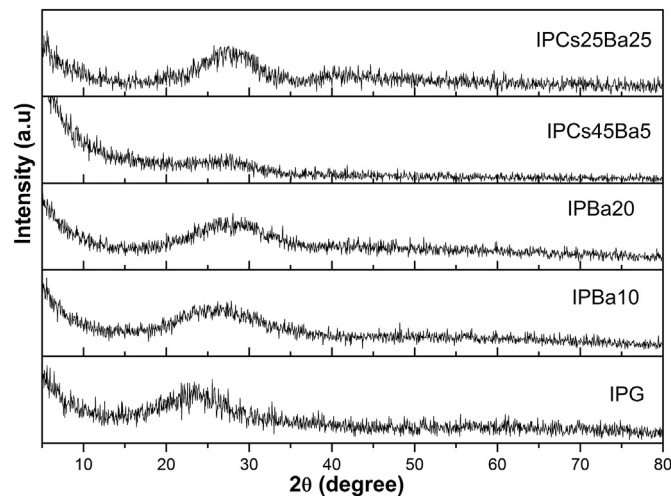


Fig. 2. XRD pattern of barium loaded iron phosphate glasses along with un-doped IPG.

temperature plays an important role in maintaining the redox (Fe^{II}/ΣFe) ratio in glass, the effect of quenching temperature on the iron redox ratio is more predominant only when quenched at a temperature higher than 1473 K [19]. As the quenching temperature of the glasses under present study was 1323 K, the reduction in quenching temperature is due to the addition of glass modifiers such as Cs₂O and/or BaO.

3.2. Density and molar volume

Table 1 shows the densities of the iron phosphate glasses under present study. Since the density of glass is sensitive to both the volume occupied by the atoms and to their atomic weight, molar volume is often used to compare the behaviour of glasses [20]. The molar mass of IPBa10 and IPBa20 are 149.5 and 149.9 g mol⁻¹ respectively, the increase being only about 0.3%. However, a greater decrease in molar volume (about 10%) was observed with increasing barium content in the glass; thus molar volume is more sensitive to change in the Ba content. Better glass network connectivity in IPBa20 compared to IPBa10 can reduce the molar volume in IPBa20. The decrease in molar volume is in agreement with similar iron phosphate glasses reported in the literature [21]. Similarly, the molecular weight of IPCs45Ba5 and IPCs25Ba25 were

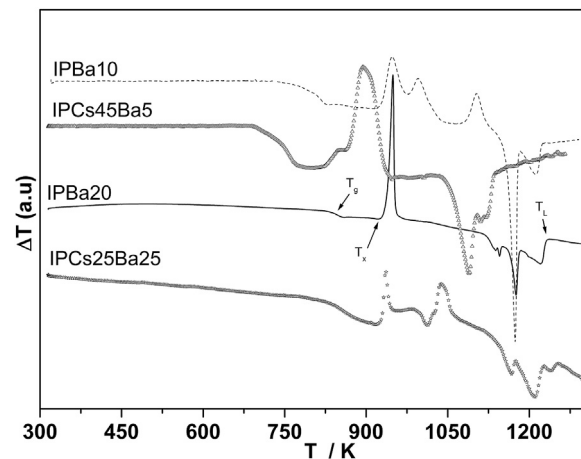


Fig. 3. DTA curves of iron phosphate glasses at 10 K/min. under flowing Ar atmosphere (20 ml/min). Typical characteristic temperatures: glass transition temperature (T_g), onset of crystallisation temperature (T_x) and liquidus temperature (T_l) are shown in the DTA curve of IPBa20.

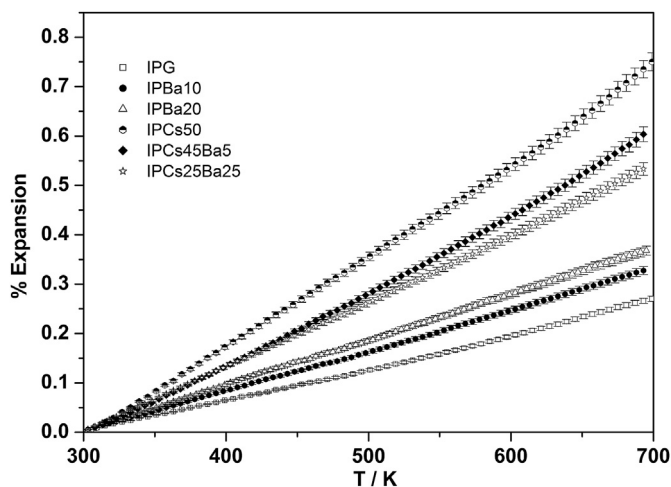


Fig. 4. Linear thermal expansion behaviour of various iron phosphate glasses.

189 and 170.3 g mol⁻¹. Although Cs and Ba have similar atomic weight, the reduction in molecular weight in IPCs25Ba25 is due to replacement of one unit of Cs₂O by a BaO. However, the density of the glass increases from IPCs45Ba5 to IPCs25Ba25, resulting in the reduction of molar volume. The molar volume of iron phosphate glass [10] containing 50 wt. % of Cs₂O (labelled as IPCs50) was 5.33×10^{-5} m³. Comparing the molar volume of IPCs50, IPCs45Ba5 and IPCs25Ba25, it is evident that the molar volume decreases when Cs is replaced by Ba, indicating the better connectivity due to better cation field strength of Ba^{II} as explained below.

3.3. Glass transition temperature

The DTA curves showing the glass transition temperature of IPBa10 and IPBa20 are shown in Fig. 3. The glass transition temperature of these glasses is also presented in Table 1. The glass transition temperature (T_g) of un-doped IPG was 783 K [13]. As the concentration of Ba increases in IPG, the glass transition temperature also increases indicating improved thermal stability. The observed increase in glass transition temperature is similar to that observed for caesium loaded IPG [10]. The T_g of 20 wt. % Cs₂O loaded IPG was 790 K. Although an increase in T_g is observed with addition of either BaO or Cs₂O, the magnitude of increase is higher (63 K) compared to that (7 K) reported for equivalent concentration of Cs₂O loaded IPG. Both Cs and Ba act as modifier in IPG but the higher glass transition temperature observed for Ba loaded IPG clearly indicates that Ba^{II} is a better glass modifier compared to Cs^I. It is well known that greater cation field strength [22] (cation charge/(radius)²) leads to a better glass network connectivity. Ba^{II} ions with cation field strength of 0.26 would have better glass network connectivity compared to Cs^I with cation field strength of 0.1. Thus, a higher glass transition temperature is observed for IPG containing Ba compared to IPG containing a similar concentration of Cs. The Crystallisation behaviour of IPBa10 is different from that of IPBa20. Multiple crystallisation exotherms are observed for

IPBa10, whereas IPBa20 shows a single crystallisation peak under similar experimental conditions. The onset temperature of the first crystallisation peak is considered as the temperature of crystallisation for IPBa10. The crystallisation temperature (T_x) of IPBa10 and IPBa20 are 910 and 923 K respectively. The observed liquidus temperatures (T_l) are 1225 and 1237 K for IPBa10 and IPBa20

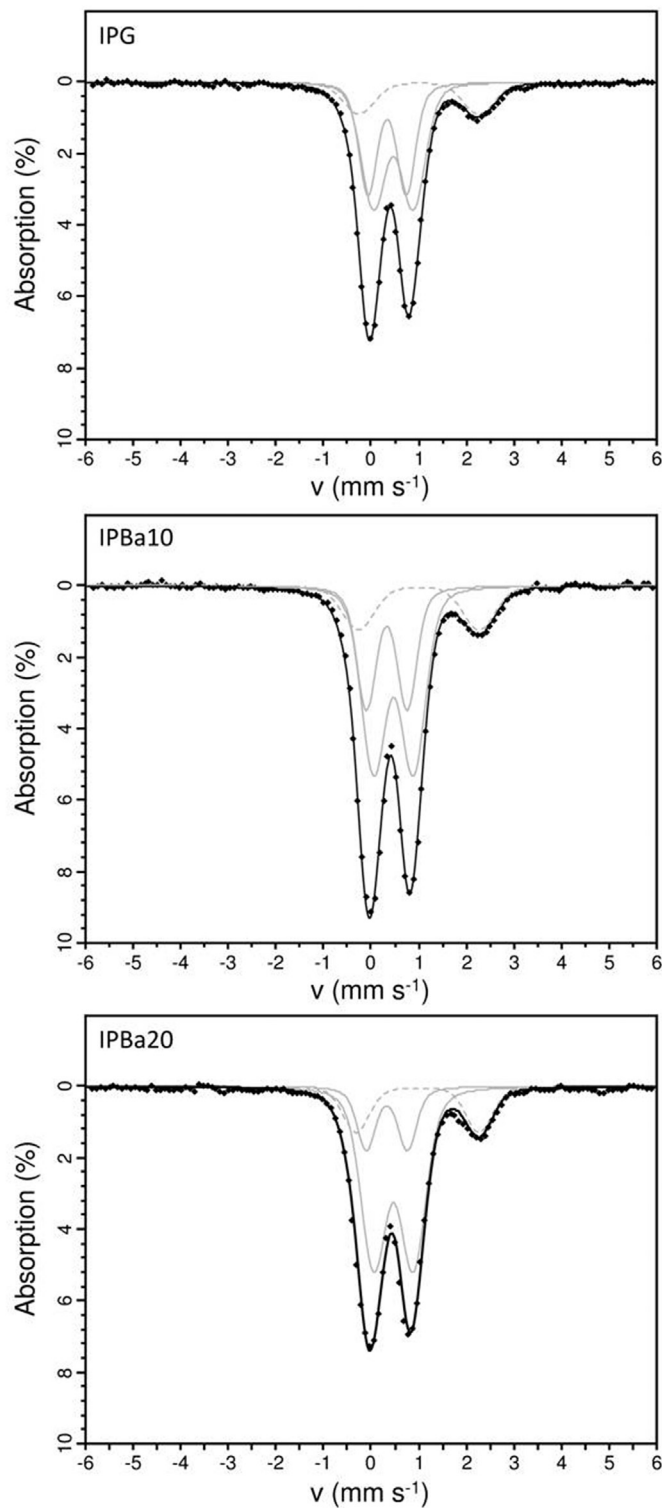


Fig. 5. Room temperature ⁵⁷Fe Mossbauer spectra of IPG, IPBa10 and IPBa20. The overall fit to the data is shown by the solid black line. Individual components are indicated by solid grey lines (Fe^{III}) or dashed grey lines (Fe^{II}).

Table 2

Values of coefficients of the quadratic fit $\frac{\Delta E}{E} \times 100 = A_1 + A_2 T + A_3 T^2$.

Sample	A ₁	A ₂	A ₃	R ²
IPBa10	-0.21023	6.73979×10^{-4}	1.46744×10^{-7}	0.999
IPBa20	-0.26833	8.99904×10^{-4}	0.23945×10^{-7}	0.999
IPCs45Ba5	-0.33012	9.1×10^{-4}	6.1853×10^{-7}	0.999
IPCs25Ba25	-0.34474	10.9×10^{-4}	2.4924×10^{-7}	0.999

respectively. The higher crystallisation temperature and liquidus temperature of IPBa20 also indicates the better stability of IPBa20 compared to IPBa10.

The glass transition temperature of IP5C5 was 743 K [10]. The glass transition temperature of 5 wt. % BaO added glass (IPCs45Ba5) showed a marginal increase in glass transition temperature, i.e., 752 K. The glass transition temperature of IPCs25Ba25 was 856 K. The increase in glass transition temperature is another indication of the better glass network connectivity or rigidity of the glass network. The increase in density (thus reduction in molar volume) and increase in glass transition temperature is a positive change when Cs is replaced by Ba. In the same way, the onset of crystallisation temperature and liquidus temperatures increases when Cs is replaced by Ba. The onset of crystallisation of IPCs45Ba5 and IPCs25Ba25 were at 802 and 920 K respectively. The liquidus temperature of IPCs45Ba5 and IPCs25Ba25 were 1142 and 1254 K respectively as shown in Fig. 3. The increase in crystallisation temperature and liquidus temperature, when Cs is replaced by Ba, also signifies the strength of the phosphate network. However, the delineation of the crystallisation behaviour of the glasses is not part of the present study.

3.4. Thermal expansion

The percentage of linear thermal expansion of IPBa10 and IPBa20 is shown in Fig. 4. The expansion of IPG [23] is also added in Fig. 4 for comparison. The thermal expansion behaviour was

experimentally determined up to 700 K, which is well below the glass transition temperature of the glasses under present study. The thermal expansion data were fitted to the quadratic equation:

$$\frac{\Delta L}{L} \times 100 = A_1 + A_2 T + A_3 T^2 \quad (1)$$

where A_1 , A_2 and A_3 are coefficients of the quadratic equation and ΔL is the change in length of the glass sample of length “L”. The values of the coefficients, A_1 , A_2 and A_3 along with R^2 values are presented in Table 2 for IPBa10 and IPBa20.

The average thermal expansion coefficient was evaluated for each glass from the plot of thermal expansion vs. Temperature as follows:

$$\alpha_{avg} = \frac{\Delta L}{L_{300K} \Delta T} \quad \text{where } \Delta L = L_{700K} - L_{300K} \text{ and } \Delta T = (700 - 300) \text{ K} \quad (2)$$

where L_{300K} and L_{700K} corresponds to the length of sample as a function of temperature at 300 and 700 K respectively. Whenever alkali oxide [21,23] or alkaline earth oxide [21] are added as modifiers in IPG, the average thermal expansion coefficient of such glass would increase compared to un-doped IPG. The values of the average thermal expansion coefficient (α_{avg}) of IPBa10 and IPBa20 are $8.22 \times 10^{-6} \text{ K}^{-1}$ and $9.31 \times 10^{-6} \text{ K}^{-1}$ respectively. The α_{avg} of IPG was $6.77 \times 10^{-6} \text{ K}^{-1}$ [21]. The expansion behaviour of Ba doped

Table 3
Room temperature Mossbauer parameters for iron phosphate glass (IPG) and Ba loaded IPG; δ – isomer shift, Δ – quadrupole splitting, Γ – full width half max, A - relative spectral area, Fe^{II} fraction ($\text{Fe}^{II}/\Sigma\text{Fe}$), and N_O - average coordination number. δ is given relative to metallic Fe at room temperature. Site assignment for each spectral contribution indicated. (IV) and (VI) indicate the coordination number of the Fe ion.

Sample	δ (mm s ⁻¹) ±0.02	Δ (mm s ⁻¹) ±0.02	Γ (mm s ⁻¹) ±0.02	A (%) ±2	Site	$\text{Fe}^{II}/\Sigma\text{Fe}$ ±0.01	N_O ±0.2
IPG	0.33	0.81	0.19	33	Fe ^{III} (IV)	0.20	5.3
	0.47	0.83	0.19	47	Fe ^{III} (VI)		
	1.00	2.51	0.19	20	Fe ^{II} (VI)		
IPBa10	0.33	0.86	0.20	27	Fe ^{III} (IV)	0.21	5.5
	0.47	0.83	0.20	52	Fe ^{III} (VI)		
	1.00	2.54	0.20	21	Fe ^{II} (VI)		
IPBa20	0.33	0.86	0.22	17	Fe ^{III} (IV)	0.22	5.7
	0.47	0.83	0.22	61	Fe ^{III} (VI)		
	0.98	2.58	0.22	22	Fe ^{II} (VI)		

Table 4
Pre-edge parameters for reference compounds, iron phosphate glass (IPG) and Ba loaded IPG. A (the summed area from all the contributions), the Fe^{II} fraction ($\text{Fe}^{II}/\Sigma\text{Fe}$) and the average coordination number (N_O) are also reported.

	Components		Centroid (eV) ±0.3	A ±0.02	N_O ±0.2	$\text{Fe}^{II}/\Sigma\text{Fe}$ ±0.05
	Centre (eV) ±0.2	Area ±0.03				
FePO ₄	7111.5	0.02	7113.3	0.33	4	0
	7113.4	0.31				
NaSiFe ₂ O ₆ (Aegerine)	7112.0	0.02	7113.4	0.09	6	0
	7112.9	0.03				
	7114.2	0.04				
FeCO ₃ (Siderite)	7111.2	0.05	7112.1	0.09	4	1
	7113.0	0.02				
	7114.0	0.01				
Fe ₂ Al ₉ O ₆ (SiO ₄) ₄ (OH) ₂ (Staurolite)	7109.1	0.01	7111.7	0.21	6	1
	7111.4	0.14				
	7112.9	0.07				
IPG	7112.0	0.04	7113.2	0.17	5.3	0.13
	7113.4	0.12				
IPBa10	7112.0	0.04	7113.1	0.16	5.4	0.20
	7113.4	0.12				
IPBa20	7112.0	0.04	7113.1	0.14	5.6	0.20
	7113.4	0.10				

glasses are higher than that of un-doped IPG, but similar to that of Cs loaded IPG reported by us earlier [21]. The average thermal expansion coefficient determined in the present study is in agreement with that reported for similar iron phosphate glasses [23]. The linear thermal expansion of IPCs45Ba5 and IPCs25Ba25 as a function of temperature is also shown in Fig. 4 along with that of IPCs50. It is apparent from the plot that as Ba replaces Cs in Cs loaded IPG, the linear thermal expansion decreases and the coefficient of the quadratic fit of these glasses are also presented in Table 2. Average thermal expansion coefficients of IPCs45Ba5 and IPCs25Ba25 are $15.3 \times 10^{-6} \text{ K}^{-1}$ and $13.4 \times 10^{-6} \text{ K}^{-1}$ respectively. These values are lower than that of IPCs50 ($19.8 \times 10^{-6} \text{ K}^{-1}$) reported earlier [21]. Similar expansion characteristics (when Ba replaces Cs completely) and reduction in thermal expansion behaviour (when Cs loaded glass is partially replaced by Ba) represent a desirable property because of the conversion of ^{137}Cs to ^{137}Ba during radioactive decay of ^{137}Cs loaded IPG. Sealed radioactive source used for clinical application would show no adverse effect due to change in thermal expansion behaviour.

3.5. ^{57}Fe Mössbauer spectroscopy

^{57}Fe Mössbauer spectra for the IPG (un-doped), IPBa10 and IPBa20 are shown in Fig. 5 along with the fitted contributions to the spectral envelope. For each glass, three contributions were fitted, indicating the presence of three distinct Fe environments which are shown as solid grey lines (Fe^{II}) or dashed grey lines (Fe^{III}) in Fig. 5 (the overall fit is shown by the solid black line). The fitted Mössbauer parameters (isomer shift – δ , quadrupole splitting – Δ , and relative spectral area - A) are shown in Table 3. In glasses, well-defined ranges of isomer shift are observed for Fe in a particular combination of oxidation state and coordination environment, allowing specific contributions to be attributed to different Fe sites [24]. Quadrupole splitting can also be used as a diagnostic for specific coordination environments, although the broad range of quadrupole splitting reported for amorphous materials, means that careful interpretation is required [24]. Ferrous ions have larger isomer shifts and quadrupole splitting than ferric ions and so are readily distinguished. Initial fitting was performed using two contributions to represent the presence of Fe^{II} and Fe^{III} species. However, more satisfactory fits were obtained by including a second Fe^{III} species, consistent with previous studies of related iron phosphate glasses, which suggested that the Fe^{III} adopts both tetrahedral and octahedral coordination [25]. The doublet centred at approximately $1.00 \pm 0.02 \text{ mm s}^{-1}$ was assigned to Fe^{II} in octahedral coordination and the doublets centred at 0.33 ± 0.02 and $0.47 \pm 0.02 \text{ mm s}^{-1}$ were assigned to Fe^{III} in tetrahedral and octahedral co-ordination, respectively. Although the measured isomer shift and quadrupole splitting for a specific combination of oxidation state and coordination number can occur over a range of values, the assignments given above are supported by published Mössbauer parameters for relevant Fe containing minerals with very well characterised structures [26–28]. The fitted ^{57}Fe Mössbauer parameters are also consistent with those previously reported in the literature for similar iron phosphate glasses [29–33]. The Fe^{II} content and the average Fe coordination numbers (N_0) were estimated, by considering the relative area of all contributions from the Fe^{II} and Fe^{III} species. In order to accurately determine the $\text{Fe}^{\text{II}}/\text{Fe}^{\text{III}}$ ratio the respective recoil free fraction ratio for ferrous (f_2) and ferric iron (f_3) need to be known. It has been assumed previously that this value is close to unity but this leads to an overestimation of the Fe^{3+} content [34]. Eeckhout and Grave [35] reported recoil free fraction ratios (f_2/f_3) of 0.734 for anapaite, $\text{Ca}_2\text{Fe}(\text{PO}_4)_2 \cdot 4\text{H}_2\text{O}$, and 0.824 for strunzite, $(\text{Mn},\text{Fe})_2(\text{PO}_4)_2(\text{OH})_2 \cdot 6\text{H}_2\text{O}$. In this study corrections were made using a value of 0.769 based on previous work on IPG

systems [36]. The isomer shift and quadrupole splitting did not vary appreciably with increasing Ba content and only a small increase in Fe^{II} iron content was observed. The estimated average Fe coordination number increased from 5.3 ± 0.2 to 5.7 ± 0.2 , with increasing Ba content, consistent with the results from the Fe K-edge XANES (X-ray absorption near edge structure) and EXAFS (extended X-ray absorption fine structure) analysis as shown in Tables 4 and 5. The presence of a contribution from five-fold coordinated Fe^{III} , was ruled out based on the reported large quadrupole splittings

Table 5

Structural parameters for iron phosphate glass (IPG) and Ba loaded IPG obtained from modelling Fe K-edge EXAFS. $R_{\text{Fe}-i}$ is the average interatomic distance for a given Fe- i pair, σ^2_i is the EXAFS Debye-Waller factor (estimated from the distribution of bond length) and $N_{\text{Fe}-i}$ is the refined number of scatterers in the coordination shell. The numbers of scatterers in the first oxygen coordination shells were allowed to refine; the number of scatterers in all other shells were fixed during the fits. The amplitude reduction factor (S_0^2), determined from the fitting of the FeCO_3 reference, was fixed at $S_0^2 = 1.033$. * indicates no calculated error as value of parameter was fixed. The same value of σ^2_{O} was used for the first two Fe-O paths. BVS is the bond valence sum for the first oxygen coordination shells.

	IPG		IPBa10		IPBa20	
		±		±		±
E_0 (eV)	1.1	1.5	4.1	1.4	3.0	1.9
$R_{\text{Fe}-\text{O}1}$ (Å)	1.90	0.01	1.93	0.01	1.95	0.01
$N_{\text{Fe}-\text{O}1}$	4.5	0.8	4.4	0.7	4.7	0.8
$R_{\text{Fe}-\text{O}2}$ (Å)	2.21	0.05	2.18	0.05	2.21	0.06
$N_{\text{Fe}-\text{O}2}$	0.6	0.8	0.9	0.4	1.0	0.7
Total N_0	5.1	1.1	5.3	0.8	5.7	1.1
Avg. R_0	1.93	0.05	1.97	0.05	1.99	0.06
σ^2_{O} (Å ²)	0.008	0.002	0.009	0.002	0.009	0.002
$\text{Fe}^{\text{II}}/\Sigma\text{Fe}$	0.12	0.10	0.17	0.10	0.18	0.10
$R_{\text{Fe}-\text{Fe}}$	2.73	0.15	2.89	0.02	2.88	0.04
$N_{\text{Fe}-\text{Fe}}$	0.5	*	0.5	*	0.5	*
$\sigma^2_{\text{Fe}}(\text{Å}^2)$	0.021	0.018	0.004	0.005	0.004	0.004
$R_{\text{Fe}-\text{P}1}$	3.15	0.02	3.26	0.18	3.27	0.41
$N_{\text{Fe}-\text{P}1}$	3	*	3	*	3	*
$R_{\text{Fe}-\text{P}2}$	3.39	0.02	3.40	0.16	3.39	0.42
$N_{\text{Fe}-\text{P}2}$	3	*	3	*	3	*
σ^2_{P} (Å ²)	0.009	0.002	0.016	0.027	0.017	0.053
$R_{\text{Fe}-\text{Ba}}$	–	–	3.07	0.05	3.09	0.03
$N_{\text{Fe}-\text{Ba}}$	–	–	0.5	*	0.5	*
σ^2_{Ba} (Å ²)	–	–	0.006	0.008	0.005	0.006
R-factor	0.008	–	0.003	–	0.028	–
BVS (v.u.)	3.1	0.6	2.9	0.6	2.9	0.6

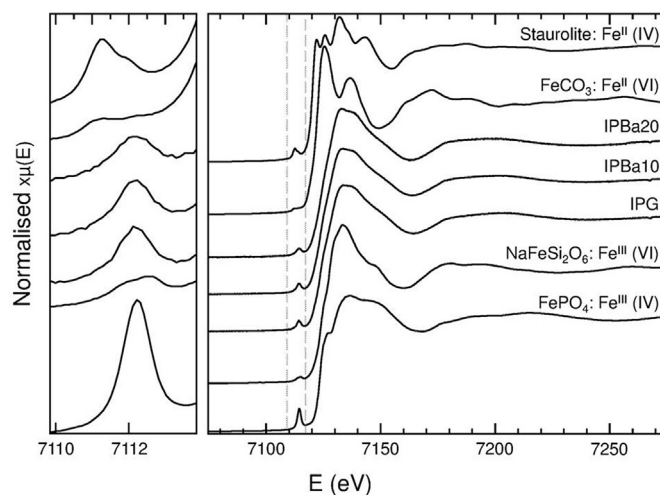


Fig. 6. Normalised Fe K-edge XANES data for IPG, IPBa10 and IPBa20. Spectra for reference materials are included. The pre-edge region is shown magnified on the left hand side of the figure.

observed for square pyramidal and trigonal bipyramidal Fe^{III} in a range of synthetic [37–40] and mineral [41,42] samples.

3.6. Fe K-edge X-ray absorption spectroscopy

3.6.1. Analysis of Fe K-edge XANES

Fig. 6 shows the Fe K-edge XANES data for the glasses under present study together with data from selected well characterised mineral and synthetic reference compounds in which the Fe oxidation state and coordination environment are known. The Fe oxidation state in the glass samples was estimated from the precise energy of the absorption edge (E_0) and interpolating between the energies measured for a set of reference compounds; a thorough treatment of this approach is given by Wong et al. [43]. In this study E_0 was set to be the energy corresponding to a normalised absorption of 0.5, after the background subtracted absorption data were normalised to a unit edge step. The measured absorption edge of the IPG glasses was $E_0 \approx 7122.8$ eV identical to that of the Fe^{III} reference compounds, and distinct from the absorption edge of Fe^{II} reference compounds at $E_0 \approx 7119.4$ eV (precision ± 0.2 eV). It is therefore clear that Fe^{III} is the dominant speciation in the IPG glasses, in agreement with analysis of ⁵⁷Fe Mössbauer data. Fine structure in the post edge region of the IPG glasses is damped compared to the crystalline reference compounds, consistent with Fe^{III} in an amorphous matrix [44], where the lack of long range order reduces coherent scattering effects.

The intensity and position of features in the pre-edge region of Fe K-edge XANES spectra, at ca. 7113 eV, provides information on both the oxidation state and the local coordination environment of Fe [44–46]. Although the area under the pre-edge peaks is strictly dependent on site symmetry, rather than coordination number, it has been shown to follow a linear relationship with average coordination number for a given Fe oxidation state [44,47]. Fitting of the pre-edge feature of the IPG glasses and reference compounds was performed in the energy range 7104 eV–7120 eV, according to the methodologies proposed by Farges and Wilke [44,46]. The background subtracted absorption data were normalised to a unit edge step using Athena [18], and the rising edge background was fitted using a spline function interpolated across the pre-edge region, as described previously [46]. Gaussian components were then fitted to the data using a least squares minimisation routine. The total area under the pre-edge feature was derived by summing the integrated intensity under each pre-edge component. In order to ensure the robustness of this fitting procedure, the values obtained for the centroid position and the integrated area of the standard compounds were compared with data previously reported by Wilke et al. [46] and Jackson et al. [48]. The validity of the fitting process used in this work was evidenced by the fact that our values and those reported in the literature were the same within experimental precision.

Table 4 summarises the fitted parameters and centroid position of the pre-edge feature (i.e. the intensity-weighted average of the energy positions of the fitted Gaussian components) for the reference compounds and the glass samples. Energy calibration was performed with respect to a Fe foil in the reference channel, with the first derivative in the edge step set to 7111.0 eV, to ensure calibration with previous studies of Fe coordination in minerals and glasses [44,46]. The centroid position of the pre-edge feature in the spectra of the iron phosphate glasses at 7113.1 ± 0.2 eV is consistent with dominant Fe^{III} speciation, when compared with the average centroid position of the Fe^{III} (7113.4 ± 0.2 eV) and Fe^{II} (7111.9 ± 0.2 eV) reference compounds, as shown in Table 4. The Fe^{II} fraction for the glass samples was estimated by interpolation between the averaged centroid positions for the Fe^{II} and Fe^{III} reference compounds. This yielded Fe^{II} contents of between $13 \pm 5\%$ and $20 \pm 5\%$ consistent with the values obtained from the Mössbauer analysis (Table 3), which is acknowledged as a more accurate probe for determination of Fe speciation [31]. Similar Fe^{II} contents (ca. 20–25%) have been reported for iron phosphate glasses of the same nominal composition; slight variations in Fe^{II} content can be attributed to the differences in melt temperature and annealing conditions employed therein [25,29,49]. The area under the pre-edge features for the glass samples is intermediate between those of the Fe^{III} reference compounds indicating an average coordination number (N_0) between four- and six-fold. Due to the pseudo-linear relationship between the area under the pre-edge and the coordination number, N_0 values for the glasses were determined by interpolating between the pre-edge areas of the Fe^{III} references. This gave average coordination numbers of between 5.3 ± 0.2 and 5.6 ± 0.2 , in excellent agreement with the analysis of Mössbauer and EXAFS data shown in Tables 3 and 4. The accuracy of the average coordination number determination for an unknown depends on the validity of the integrated areas extracted from fitting of the standard compounds. The absolute differentiation between the Fe^{II} compounds with tetrahedral and octahedral coordination, estimated as the area under the pre-edge feature, was 0.24 (in arbitrary units). A similar value of 0.24 units was reported for Wilke et al. [46] and Jackson et al. [48] giving us confidence in our extracted average coordination numbers.

3.6.2. Analysis of Fe K-edge EXAFS

The local co-ordination environment of Fe in the iron phosphate glasses was further investigated by analysis of the Fe K-edge EXAFS data. Accurate determination of first shell coordination number (N_0) in amorphous materials requires independent determination of the amplitude reduction factor (S_0^2), since this is directly correlated with N_0 [50]. In general, it is assumed that the value of S_0^2 is transferrable between materials for a given element studied at the same beamline [50]. Consequently we independently determined a value for $S_0^2 = 1.03$ from fitting EXAFS data acquired for FeCO₃

Table 6

Structural parameters for FeCO₃ reference obtained from Fe K-edge EXAFS fits. R_{Fe-i} is the average interatomic distance for a given Fe-i pair, σ_i^2 is the EXAFS Debye-Waller factor (estimated from the distribution of bond length) and N_{Fe-i} is the coordination number (fixed in the model). The refined amplitude reduction factor (S_0^2) was $S_0^2 = 1.033$. The fit range in k was from 3.0 to 11.0 Å⁻¹ and in R from 1.0 to 4.5 Å. The number of independent variables (N_v) and data (N_{ip} , determined from the Nyquist theorem) was $N_v = 8$ and $N_{ip} = 17.5$, respectively.

FeCO ₃	R-factor	±	ΔE_0	±	R_{Fe-i}	±	σ_i^2	±	N_{Fe-i}	±	BVS	±
	0.017	0.001	1.77	1.23	–	–	–	–	–	–	–	–
Fe-O1	–	–	–	–	2.11	0.01	0.009	0.002	6	–	1.8	0.4
Fe-C	–	–	–	–	2.96	0.03	0.004	0.003	6	–	–	–
Fe-O2	–	–	–	–	3.14	0.03	0.009	0.002	6	–	–	–
Fe-Fe1	–	–	–	–	3.73	0.02	0.010	0.002	6	–	–	–
Fe-O3	–	–	–	–	3.95	0.02	0.009	0.002	12	–	–	–
Fe-O4	–	–	–	–	4.39	0.05	0.009	0.002	6	–	–	–
Fe-Fe2	–	–	–	–	4.63	0.03	0.06	0.03	6	–	–	–

(siderite) using the structural model reported by Effenberger [51]; the fitted model parameters are reported in Table 6. The refined Fe-O contact distance, $2.11 \pm 0.01 \text{ \AA}$, was in agreement with that reported by Effenberger, and the determined bond valence sum (BVS, [52]) was $1.8 \pm 0.4 \text{ v.u.}$, consistent with speciation as Fe^{II} .

Inspection of the extracted EXAFS data from the iron phosphate glasses (Fig. 7) showed a simplified and damped waveform, consistent with an amorphous material [50]. The model elaborated to fit the Fe K-edge EXAFS data comprised several distinct

scattering paths, based on the crystal structure of $\text{Fe}_3(\text{P}_2\text{O}_7)_2$ [53] which has been shown to crystallise as the primary phase from these IPG glasses upon heat treatment [19,32,49]. Previous X-ray and neutron scattering studies of IPG have shown the average local Fe environment to be approximated by those in $\text{Fe}_3(\text{P}_2\text{O}_7)_2$ [54].

All Fe K-edge EXAFS data were modelled using an amplitude reduction factor of $S_0^2 = 1.03$, as noted above. The $k^2\chi(k)$ waveforms and FT $k^2\chi(k)$ plots, together with theoretical fits, are shown in Fig. 7. The refined structural parameters for all the glasses are

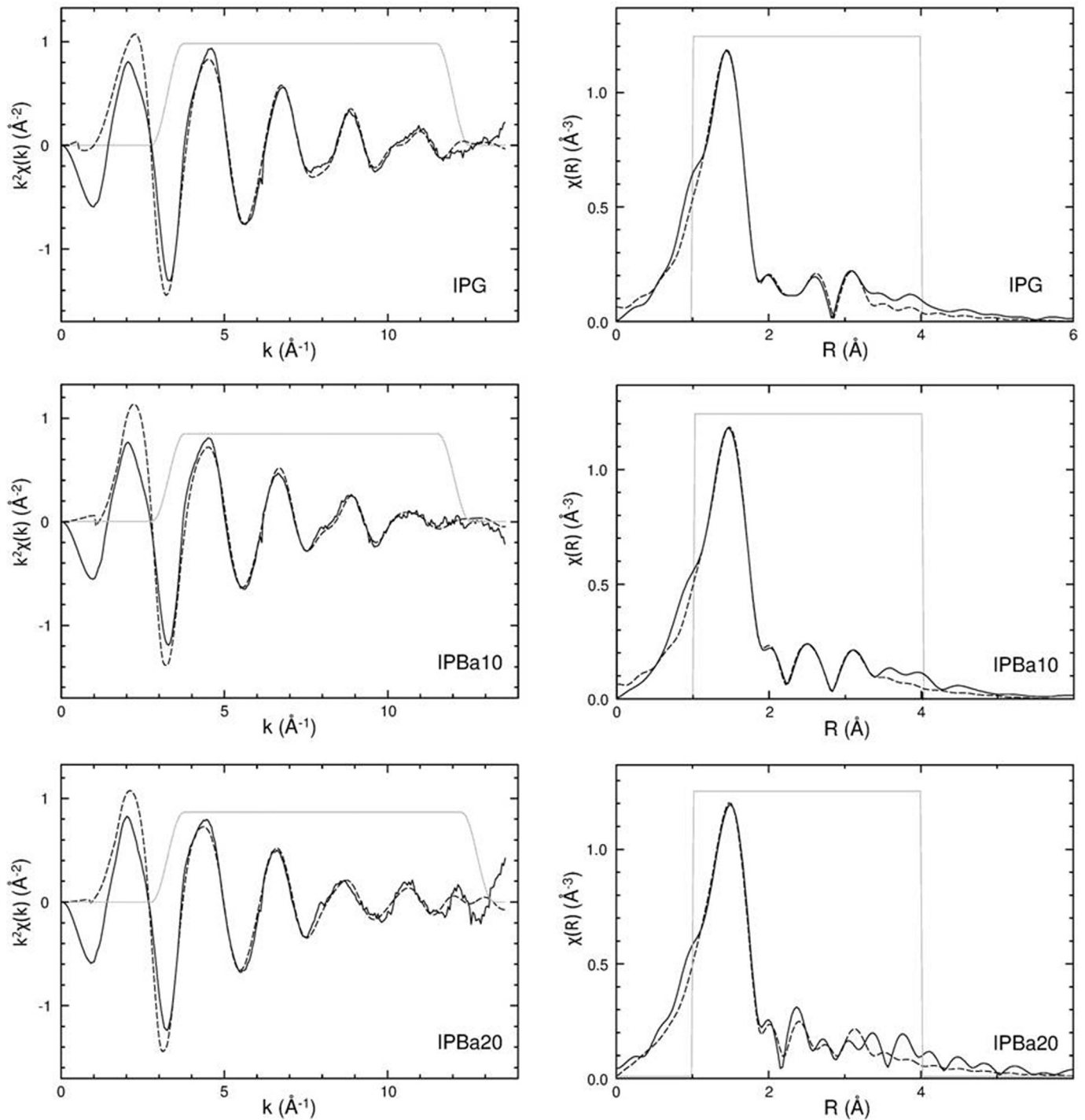


Fig. 7. $k^2\chi(k)$ and FT of $k^2\chi(k)$ Fe K-edge EXAFS data of IPG and Ba loaded IPG (uncorrected for phase shift). Solid black lines represent experimental data and dashed black lines represent theoretical fits. Fitting windows are indicated by solid grey lines.

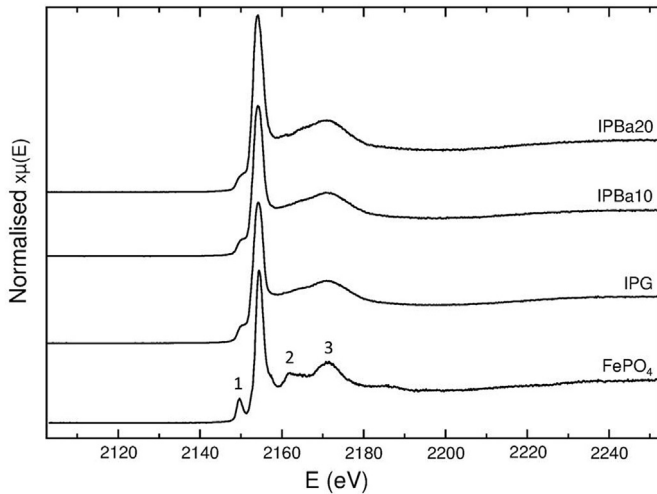


Fig. 8. Normalised P K-edge XANES data for IPG, Ba loaded IPG, and FePO₄ reference material.

summarised in Table 5. Taking the analysis of IPBa10 as an example, the most significant modelled contributions to the EXAFS data were associated with two distinct Fe-O contact distances at ca. $R_{\text{Fe-O1}} = 1.93 \pm 0.01 \text{ \AA}$ (with $N_{\text{Fe-O1}} = 4.4 \pm 0.7$) and ca. $R_{\text{Fe-O2}} = 2.18 \pm 0.05 \text{ \AA}$ with ($N_{\text{Fe-O2}} = 0.9 \pm 0.4$). These two Fe-O contact distances are characteristic of Fe^{III} and Fe^{II} species, respectively. The estimated Fe^{II}/ΣFe ratio (0.17 ± 0.10), calculated from the EXAFS contact distances, is in good agreement with that determined by fitting of the pre-edge XANES features (0.20 ± 0.05) and the Mössbauer data (0.21 ± 0.01). The average Fe-O co-ordination number determined from modelling the EXAFS data was 5.3 ± 0.8 , again in good agreement with that estimated from analysis of XANES (5.4 ± 0.2) and Mössbauer data (5.5 ± 0.2). The crystal structure of Fe₃(P₂O₇)₂ is characterised by an Fe₃O₁₂ cluster consisting of a Fe^{II} trigonal prism (Fe-O, ca. 2.11 Å) and two Fe^{III} octahedra (Fe-O ca. 2.00 Å) connected by a pyrophosphate (P₂O₇)⁴⁻ group [49,53]. Our EXAFS determined Fe-O contact distances are therefore in reasonable agreement with those reported for the model Fe₃(P₂O₇)₂ compound; the shorter Fe-O contact distance for Fe^{III} reported here is consistent with the observation of ferric iron tetrahedra in our glasses.

Previous studies of glasses with similar compositions, have reported models based on three distinct Fe-O contact distances representing both tetrahedral and octahedral Fe^{III} and octahedral Fe^{II} [25,30,31,33,49]. Attempts to model our data using three Fe-O contact distances proved unsuccessful. Our average Fe-O contact distances were validated by calculation of the bond valence sum [52], using the refined coordination number (N_{O}), giving values of ca. $3.0 \pm 0.6 \text{ v.u.}$, consistent with the presence of majority Fe^{III} in the

glass samples.

As shown in Fig. 7, the FT $k^2\chi(k)$ data show significant features in the range $R = 2.1\text{--}3.9 \text{ \AA}$, uncorrected for phase shift. For all the glasses, these features were fitted by one Fe-Fe path at $R_{\text{Fe-Fe}} \approx 2.8 \text{ \AA}$ (with $N_{\text{Fe-Fe}} = 0.5$) and two Fe-P paths, one each at ca. $R_{\text{Fe-P1}} \approx 3.2 \text{ \AA}$ and $R_{\text{Fe-P2}} \approx 3.4 \text{ \AA}$ (with $N_{\text{Fe-P1}} = 3.0$ and $N_{\text{Fe-P2}} = 3.0$). An attempt to fit a single Fe-P path at an intermediate distance was unsuccessful; the relative precision on the determined Fe-P contact distances confirms the presence of two distinct contributions, at least for the Ba free composition. The refined Fe-P and Fe-Fe contact distances are commensurate with those reported in Fe₃(P₂O₇)₂ [53], which are distributed about values of ca. 3.3 Å and 2.9 Å, respectively. Addition of these paths typically reduced the residual R-factor by ca. 75%, associated with satisfactory fitting of the weak but significant FT $k^2\chi(k)$ features in the range $R = 2.1\text{--}3.9 \text{ \AA}$. In the case of Ba doped compositions, it was possible to fit an additional Fe-Ba path at ca. 3.0 Å with $N_{\text{Fe-Ba}} = 0.5$, which further improved the fit to FT $k^2\chi(k)$ features in the range $R = 2.1\text{--}3.9 \text{ \AA}$. Attempts to refine the weighting of the Fe-P, Fe-Fe and Fe-Ba path lengths, even under heavy damping, were unsuccessful, but this is understandable given the amorphous nature of the material. Adjustment of the constrained weighting of these paths, in steps of $N = 0.5$, afforded a progressive increase in the residual R-factor and ultimately an implausible model.

3.7. P K-edge X-ray absorption spectroscopy

3.7.1. Analysis of P K-edge XANES

Fig. 8 shows the P K-edge XANES data for the IPG glasses together with data from the synthetic FePO₄ reference compound for which the P oxidation state and co-ordination environment are known. The absorption edge of the iron phosphate glasses was determined to be $E_0 \approx 2152.7 \text{ eV}$, close to that of the P^V reference compound (FePO₄) at $E_0 \approx 2152.5 \text{ eV}$. The P-K edge XANES spectra of Fe-phosphate minerals have a very distinct pre-edge feature on the low energy side of the intense white line at ca. 2150 eV [55–57] which is clearly apparent in our reference data (labelled feature 1 in Fig. 8). In the iron phosphate glass samples this pre-edge feature is present as a broad shoulder rather than as a distinct and well-defined feature. Additionally, the features in the XANES region (labelled features 2 and 3) are weaker, relative to the absorption edge, than in the crystalline reference material. This damping of the fine structure in the glass samples is consistent with P in an amorphous matrix [44] and similar spectra have been reported in the literature for sodium polyphosphate glass [58] and amorphous SiO₂-P₂O₅ materials [59]. Comparison with the FePO₄ reference, presented here, and also reference spectra for Na₄P₂O₇ and Na₃P₃O₉ [58] indicate that the IPG glass structure consists of a network of pentavalent phosphorus tetrahedra, most likely speciated as pyrophosphate (P₂O₇)⁴⁻ groups.

Table 7

Structural parameters for FePO₄ reference obtained from P K-edge EXAFS fits. $R_{\text{p-i}}$ is the average interatomic distance for a given P-i pair, σ^2_i is the EXAFS Debye-Waller factor (estimated from the distribution of bond length) and $N_{\text{p-i}}$ is the refined coordination number (fixed in the model). The refined amplitude reduction factor (S^2_0) was $S^2_0 = 0.785$. The fit range in k was from 3.5 to 11.0 Å⁻¹ and in R from 0.8 to 5.0 Å. The number of independent variables (N_v) and data (N_{ip} , determined from the Nyquist theorem) was $N_v = 10$ and $N_{\text{ip}} = 19.6$, respectively.

FePO ₄	R-factor	±	ΔE ₀	±	R _{p-i}	±	σ ² _i	±	N _{p-i}	±	BVS	±
	0.162	0.006	3.57	4.91	–	–	–	–	–	–	–	–
P-O1	–	–	–	–	1.52	0.02	0.004	0.003	4	–	5.2	1.0
P-O-O-P	–	–	–	–	2.94	0.02	0.008	0.006	16	–	–	–
P-Fe	–	–	–	–	3.11	0.06	0.008	0.007	4	–	–	–
P-O2	–	–	–	–	3.56	0.08	0.004	0.003	6	–	–	–
P-O3	–	–	–	–	4.17	0.09	0.004	0.003	14	–	–	–
P-P	–	–	–	–	4.16	0.12	0.009	0.002	4	–	–	–

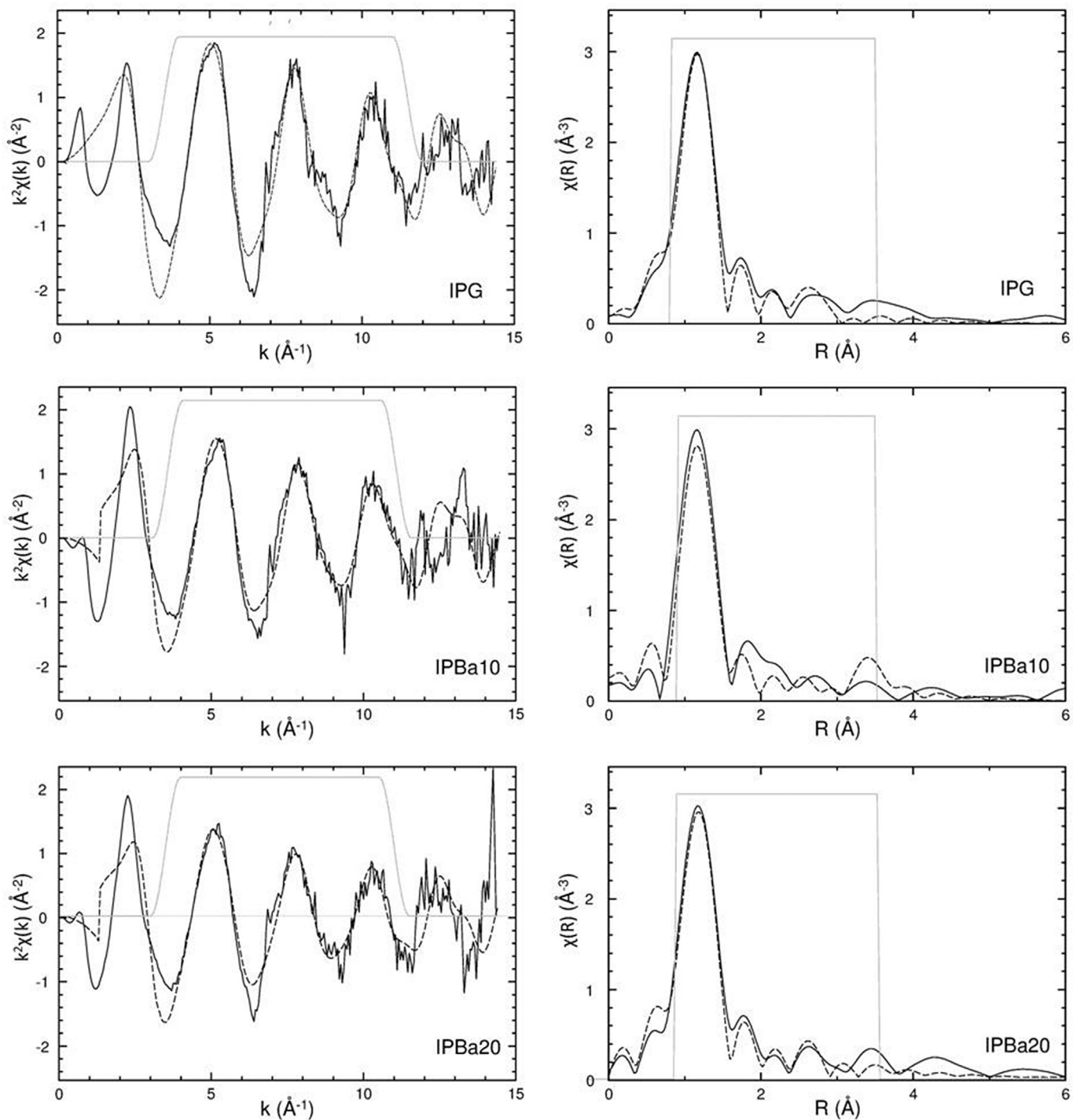


Fig. 9. $k^2\chi(k)$ and FT of $k^2\chi(k)$ P K-edge EXAFS data of IPG and Ba loaded IPG (uncorrected for phase shift). Solid black lines represent experimental data and dashed black lines represent theoretical fits. Fitting windows are indicated by solid grey lines.

3.7.2. Analysis of P K-edge EXAFS

The local co-ordination environment of P in the iron phosphate glasses was investigated by analysis of the P K-edge EXAFS data. A value for $S_0^2 = 0.785$ was determined from fitting EXAFS data acquired for FePO_4 using the structural model reported by Labeguerie [60]; the fitted model parameters are reported in Table 7. The refined P-O contact distance, $2.51 \pm 0.01 \text{ \AA}$, was in agreement with that reported by Labeguerie; the calculated BVS was $5.3 \pm 1.0 \text{ v.u.}$

consistent with speciation as P^{V} .

Inspection of the extracted EXAFS data from the IPG, and Ba loaded IPG glasses (Fig. 9), showed a simplified and damped waveform, with no distinct features corresponding to medium range order, consistent with an amorphous material [50]. The model elaborated to fit the EXAFS data comprises several distinct scattering paths, based on the crystal structure of $\text{Fe}_3(\text{P}_2\text{O}_7)_2$ [53] which contains pyrophosphate $(\text{P}_2\text{O}_7)^{4-}$ groups. The EXAFS data

Table 8

Structural parameters for iron phosphate glass (IPG) and Ba loaded IPG obtained from P K-edge EXAFS fits. R_{p-i} is the average interatomic distance for a given P-i pair, σ^2_i is the EXAFS Debye-Waller factor (estimated from the distribution of bond length) and N_{p-i} is the refined number of scatterers in the coordination shell. The number of scatterers in the first oxygen coordination shell was allowed to refine; the number of scatterers in all other shells were fixed during the fits. The amplitude reduction factor (S^2_0), determined from the fitting of the $FePO_4$ reference, was fixed at $S^2_0 = 0.785$. * indicates no calculated error as value of parameter was fixed. The same value of σ^2_O was used for both Fe-O paths. BVS is the bond valence sum for the first oxygen coordination shell.

	IPG		IPBa10		IPBa20	
		±		±		±
E_0 (eV)	0.4	4.5	3.1	4.2	6.6	4.3
R_{p-O1} (Å)	1.51	0.02	1.51	0.02	1.53	0.02
N_{p-O1}	4.1	0.8	4.1	0.5	4.00	0.4
σ^2_O (Å ²)	0.001	0.002	0.001	0.002	0.001	0.002
R_{p-Fe} (Å)	3.12	0.05	3.17	0.10	3.13	0.05
N_{p-Fe}	4.0	*	4.0	*	4.0	*
σ^2_{Fe} (Å ²)	0.005	0.003	0.018	0.014	0.006	0.003
R_{p-O2}	3.27	0.07	3.82	0.07	3.29	0.06
N_{p-O2}	6.0	*	6.0	*	6.0	*
R-factor	0.052	—	0.059	—	0.045	—
BVS (v.u.)	5.3	1.0	5.3	1.0	5.1	1.0

were modelled using an amplitude reduction factor of $S^2_0 = 0.785$, as noted above. The $k^2\chi(k)$ waveforms and FT $k^2\chi(k)$ plots, together with theoretical fits, are shown in Fig. 9 and the refined structural parameters for all the glasses are summarised in Table 8. A single P-O shell was used to model the intense feature in the EXAFS envelope at ca. 1.2 Å (uncorrected for phase shift). Refinement of the contact distance yielded an R_{p-O1} value of ca. 1.52 ± 0.02 Å and a corresponding coordination number (N_{p-O1}) of 4.1 ± 0.8 . The crystal structure of $Fe_3(P_2O_7)_2$ is characterised by Fe_3O_{12} clusters connected by a pyrophosphate (P_2O_7)⁴⁻ group (with a P-O bond length of 1.53 Å) [50,53]. Our EXAFS determined P-O contact distances are therefore in excellent agreement with those reported for the model $Fe_3(P_2O_7)_2$ compound. Calculation of the BVS based on a P-O contact of ca. 1.51 gave a value of 5.3 ± 1.0 v.u. as expected for P^V . Small but significant improvement was achieved by the inclusion of two additional shells; a P-Fe path at ca. $R_{p-Fe} \approx 3.1$ Å (with $N_{p-Fe} = 4$) and an additional P-O path at ca. $R_{p-O2} \approx 3.3$ Å (with $N_{p-O2} = 6$). Attempts to refine the weightings for these paths proved unsuccessful.

4. Conclusions

Iron phosphate glasses containing either BaO loaded or Cs_2O /BaO were synthesised without phase separation or crystallisation. An increase in glass transition temperature with the addition of BaO in IPG or Cs_2O loaded IPG indicates the better glass rigidity or glass network connectivity compared to that of un-doped IPG. Similar thermal expansion behaviour of IPG loaded with either Cs [20] or Ba suggest that no adverse effect would result when caesium loaded iron phosphate glass is completely converted to barium loaded iron phosphate glass, a promising result for the use of ¹³⁷Cs loaded IPG as radioactive source for medical applications. Investigation of the glass structure by Mössbauer, EXAFS and XANES also rules out any drastic modification as a result of large scale Ba doping in IPG. The isomer shift and quadrupole splitting did not vary appreciably with increasing Ba content and only a small increase in Fe^{II} content was observed. The average coordination number for IPG was 5.3 ± 0.2 and increased to 5.7 ± 0.2 with increasing Ba content. The average coordination number, Fe^{II} content in these iron phosphate glasses obtained by various techniques (Mössbauer and X-ray absorption spectroscopy) were found to be in good agreement with each other.

Acknowledgements

The authors gratefully acknowledge Diamond Light Source for time on B18 under proposals SP6871 and SP9489. Use of the National Synchrotron Light Source, Brookhaven National Laboratory, was supported by the U.S. Department of Energy, Office of Science, Office of Basic Energy Sciences, under Contract No. DE-AC02-98CH10886. This work was supported in part by EPSRC under grants EP/I012214/1 and EP/K007882/1. Neil C. Hyatt is grateful to The Royal Academy of Engineering and Nuclear Decommissioning Authority for support. This work was, in part, performed in the MIDAS Facility at The University of Sheffield, for which the financial support of the Department of Energy and Climate Change is gratefully acknowledged. Kitheri Joseph is grateful to authorities of the Department of Atomic Energy for allowing her on deputation to the UK. The authors thank Sajal Ghosh of the Chemistry Group, IGCAR for his help in obtaining the DTA data.

References

- [1] D.E. Day, Z. Wu, C.S. Ray, P. Hrma, Chemically durable iron phosphate glass waste forms, *J. Non-Cryst. Solids* 241 (1998) 1–12.
- [2] J.M. Perez Jr., D.F. Bickford, D.E. Day, D.S. Kim, S.L. Lambert, S.L. Marra, D.K. Peeler, D.M. Strachan, M.B. Triplett, J.D. Vienna, R.S. Wittman, High Level Waste Melter Study Report, Pacific Northwest National Laboratory Report, PNNL-13582, 2001.
- [3] D.E. Day, C.S. Ray, C.W. Kim, Final Report: Iron Phosphate Glasses: An Alternative for Vitrifying Certain Nuclear Wastes, Project No. DE-FG07-96ER45618, 2004.
- [4] D. Zhu, C.W. Kim, D.E. Day, Corrosion behaviour of inconel 690 and 693 in an iron phosphate melt, *J. Nucl. Mat.* 336 (2005) 47–53.
- [5] C.M. Jantzen, Historical development of glass and ceramic waste forms for high level radioactive wastes (Chapter 6) in: M.I. Ojovan (Ed.), *Handbook of Advanced Radioactive Waste Conditioning Technologies*, 2011, p. 167. Woodhead, Cambridge.
- [6] C.M. Jantzen, Development of glass matrices for high level radioactive wastes (Chapter 9) in: M.I. Ojovan (Ed.), *Handbook of Advanced Radioactive Waste Conditioning Technologies*, 2011, p. 277. Woodhead, Cambridge.
- [7] C.W. Kim, C.S. Ray, D. Zhu, D.E. Day, D. Gombert, A. Aloy, A. Mogus-Milankovic, M. Karabulut, Chemically durable iron phosphate glasses for vitrifying sodium bearing waste (SBW) using conventional and cold crucible induction melting (CCIM) techniques, *J. Nucl. Mat.* 322 (2003) 152–164.
- [8] W. Huang, D.E. Day, C.S. Ray, C.W. Kim, High temperature properties of an iron phosphate melt containing high chrome nuclear waste, *J. Nucl. Mat.* 346 (2005) 298–305.
- [9] S.L. Lambert, D.S. Kim, Tank Waste Remediation System High-level Waste Feed Processability Assessment Report", Pacific Northwest National Laboratory Report, PNNL- #WHC-SP-1143, 1994.
- [10] Kitheri Joseph, K.V. Govindan Kutty, P. Chandramohan, P.R. Vasudeva Rao, Studies on the synthesis and characterization of caesium-containing iron phosphate glasses, *J. Nucl. Mat.* 384 (2009) 262–267.
- [11] Sharing Innovative Experiences, Fighting cancer with Caesium, India, in: *Examples of Successful Initiatives in Science and Technology in the South*, vol. 1, Published in partnership with Third World Academy of Sciences (TWAS) and Third World Network of Scientific Organisation (TWNISO), 1999, p. 138.
- [12] M.I. Ojovan, W.E. Lee, *An Introduction to Nuclear Waste Immobilization*, second ed., Elsevier, Amsterdam, 2014.
- [13] Kitheri Joseph, Sajal Ghosh, K.V. Govindan Kutty, P.R. Vasudeva Rao, Crystallization kinetics, stability and glass forming ability of iron phosphate and caesium loaded iron phosphate glasses, *J. Nucl. Mater.* 426 (2012) 233–239.
- [14] K.V. Govindan Kutty, R. Asuvathraman, M.V. Krishnaiah, V. Ganesan, R. Parthasarathy, D. Sai Subalakshmi, B. Suhasini, K.C. Srinivas, K.A. Gopal, P.V. Kumar, Design, Fabrication and Commissioning of a Push Rod Dilatometer for Thermal Expansion Studies on Solids, Report IGC-283, Indira Gandhi Centre for Atomic Research, Kalpakkam 603 102, India, 2006.
- [15] K. Lagarec, D.G. Rancourt, Recoil. Mossbauer Spectral Analysis Software for Windows, University of Ottawa, Ottawa, 1998.
- [16] S.D. Forder, O.M. Hannant, P.A. Bingham, R.J. Hand, *J. Phys. Conf. Ser.* 217 (2010) 012072.
- [17] J.C. Woicik, B. Ravel, D.A. Fischer, W.J. Newburgh, Performance of a four-element Si drift detector for X-ray absorption fine structure spectroscopy: resolution, maximum count rate, and dead time correction with incorporation in to the ATHENA data analysis software, *J. Synchrotron Rad.* 17 (2010) 409–413.
- [18] B. Ravel, M. Newville, ATHENA, ARTEMIS, HEPHAESTUS: data analysis for X-ray absorption spectroscopy using IFFFIT, *J. Synchrotron Rad.* 12 (2005) 537–541.
- [19] C.S. Ray, X. Fang, M. Karabulut, G.K. Marasinghe, D.E. Day, Effect of melting temperature and time on iron valence and crystallisation of iron phosphate

- glasses, *J. Non. Cryst. Solids* 249 (1999) 1–16.
- [20] J.E. Shelby, *Introduction to Glass Science and Technology*, second ed., 2005, p. p139. RS. C.
- [21] P.A. Bingham, R.J. Hand, O.M. Hannant, S.D. Forder, S.H. Kilcoyne, Effects of modifier additions on the thermal properties, chemical durability, oxidation state and structure of iron phosphate glasses, *J. Non-Cryst. Solids* 355 (2009) 1526–1538.
- [22] Lina Ma, R.K. Brow, Amitava Choudhury, Structural study of $\text{Na}_2\text{O}-\text{FeO}-\text{Fe}_2\text{O}_3-\text{P}_2\text{O}_5$ glasses by Raman and Mössbauer spectroscopy, *J. Non-Cryst. Solids* 402 (2014) 64–73.
- [23] Kitheri Joseph, R. Asuvathraman, R. Venkata Krishnan, Jose Joseph, K.V. Govindan Kutty, P.R. Vasudeva Rao, Investigation of thermal expansion and specific heat of caesium loaded iron phosphate glasses, *J. Nucl. Mat.* 429 (2012) 1–6.
- [24] M. Darby Dyar, A review of Mossbauer data on inorganic glasses: the effects of composition on iron valency and coordination, *Am. Mineral.* 70 (1985) 304–316.
- [25] M. Karabulut, G.K. Marasinghe, C.S. Ray, D.E. Day, G.D. Waddill, C.H. Booth, P.G. Allen, J.J. Bucher, D.L. Calder, D.K. Shuh, An investigation of the local iron environment in iron phosphate glasses having different Fe(II) concentrations, *J. Non. Cryst. Solids* 306 (2002) 182–192.
- [26] J.M. Millet, C. Virely, M. Forissier, P. Bussiere, J.C. Vadrine, Mossbauer spectroscopic study of iron phosphate catalysts used in selective oxidation, *Hyp. Int.* 46 (1989) 619–628.
- [27] X. Yu, D.E. Day, G.J. Long, R.K. Brow, Properties and structure of sodium-iron phosphate glasses, *J. Non Cryst. Solids* 215 (1997) 21–31.
- [28] E. Schmidbauer, Th. Kunzmann, Electrical conductivity, thermopower and ^{57}Fe Mossbauer spectroscopy of aegirine, *Phys. Chem. Miner.* 31 (2004) 102–114.
- [29] M. Karabulut, G.K. Marasinghe, C.S. Ray, D.E. Day, G.W. Waddill, P.G. Allen, C.H. Booth, J.J. Bucher, D.L. Caulder, D.K. Shuh, M. Grimsditch, M.-L. Saboungi, Local environment of iron and uranium ions in vitrified iron phosphate glasses studied by Fe K and U L_{III} edge X-ray absorption fine structure spectroscopy, *J. Mat. Res.* 15 (2000) 1972–1984.
- [30] G.K. Marasinghe, M. Karabulut, C.S. Ray, D.E. Day, D.K. Shuh, P.G. Allen, M.L. Saboungi, M. Grimsditch, D. Haefner, Properties and structure of vitrified iron phosphate nuclear wasteforms, *J. Non. Cryst. Solids* 263–264 (2000) 146–154.
- [31] G.K. Marasinghe, M. Karabulut, C.S. Ray, D.E. Day, M.G. Shumsky, W.E. Yelon, C.H. Booth, P.G. Allen, D.K. Shuh, Structural features of iron phosphate glasses, *J. Non. Cryst. Solids* 222 (1997) 144–152.
- [32] M. Karabulut, B. Yuce, O. Bozdogan, H. Ertap, G.M. Mammadov, Effect of boron addition on the structure and properties of iron phosphate glasses, *J. Non. Cryst. Solids* 357 (2011) 1455–1462.
- [33] Y. Lin, Y. Zhang, W. Huang, K. Lu, Y. Zhao, Structural studies of iron in phosphate glasses, *J. Non. Cryst. Solids* 112 (1989) 136–141.
- [34] E. De Grave, A. Van Alboom, Evaluation of ferrous and ferric Mossbauer fractions, *Phys. Chem. Miner.* 18 (1991) 337–342.
- [35] S.G. Eeckhout, E. De Grave, Evaluation of ferrous and ferric Mossbauer fractions. Part II, *Phys. Chem. Miner.* 30 (2003) 142–146.
- [36] P.A. Bingham, S.D. Forder, R.J. Hand, A. Lavaysierre, Mossbauer studies of phosphate glasses for the immobilisation of toxic and nuclear wastes, *Hyp. Int.* 165 (2005) 135–140.
- [37] A. Modaressi, A. Courtois, R. Gerardin, B. Malaman, C. Gleitzer, Fe_3PO_7 , Un cas de coordination 5 du fer trivalent, etude structural et magnetique, *J. Solid State Chem.* 47 (1983) 245–255.
- [38] P.M. Rao, A. Gerard, F. Grandjean, Mossbauer study of the hexagonal ferrite series $\text{SrFe}_{12-x}\text{Cr}_x\text{O}_{19}$, *J. Magn. Mag. Mat.* 15–18 (1980) 645–646.
- [39] A. Bustamante, L. De Los Santos Valladares, J. Flores, C.H.W. Barnes, Y. Majima, Aging effect in $\text{CaLaBa}[\text{Cu}_{1-x}\text{Fe}_x]_3\text{O}_{7-\delta}$ with $0 \leq x \leq 0.07$ studied by Mossbauer spectroscopy, *Hyper. Int.* 203 (2011) 119–124.
- [40] M. Sarkar, N.V. Patel, P.K. Mehta, D.R.S. Somayajulu, Mossbauer study of multiple substitutions in YBCO, *Hyper. Int.* 136–137 (2001) 587–592.
- [41] J.C. Waerenborgh, M.O. Figueiredo, X-ray powder diffraction and ^{57}Fe Mossbauer spectroscopy study of the thermal breakdown of vivianite, $\text{Fe}_3(\text{PO}_4)_2 \cdot 8\text{H}_2\text{O}$, *Hyper. Int.* 29 (1986) 1101–1104.
- [42] M. Nasraoui, J.C. Waerenborgh, Fe speciation in weathered pyrochlore-group minerals from the Lueshe and Araxa (Barreiro) carbonatites by ^{57}Fe Mossbauer spectroscopy, *Can. Mineral.* 39 (2001) 1073–1080.
- [43] J. Wong, F.W. Lytle, R.P. Messmer, D.H. Maylotte, K-edge absorption spectra of selected vanadium compounds, *Phys. Rev. B* 30 (1984) 5596–5610.
- [44] F. Farges, Y. Lefrere, S. Rossano, A. Berthereau, G. Calas, G.E. Brown Jr., The effect of redox state on the local structural environment of iron in silicate glasses: a combined XAFS spectroscopy, molecular dynamics, and bond valance study, *J. Non. Cryst. Solids* 344 (2004) 176–188.
- [45] G. Giuli, G. Pratesi, S.G. Eeckhout, C. Koeberl, E. Paris, Iron reduction in silicate glass produced during the 1945 nuclear test at the Trinity site (Alamogordo, New Mexico, USA), in: R.L. Gibson, W.U. Reimold (Eds.), *Large Meteorite Impacts and Planetary Evolution IV*, vol. 465, Geological Society of America Special Paper, 2010, pp. 653–660.
- [46] M. Wilke, F. Farges, P.-E. Petit, G.E. Brown Jr., F. Martin, Oxidation state and coordination of Fe in minerals: an Fe K-XANES spectroscopic study, *Am. Mineral.* 86 (2001) 714–730.
- [47] M. Abuin, A. Serrano, J. Chaboy, M.A. Garcia, N. Carmona, XAS study of Mn, Fe and Cu as indicators of historical glass decay, *J. Anal. At. Spectrom.* 28 (2013) 1118–1124.
- [48] W.E. Jackson, F. Farges, M. Yeager, P.A. Mabrouk, S. Rossano, G.A. Waychunas, E.I. Solomon, G.E. Brown Jr., Multi-spectroscopic study of Fe(II) in silicate glasses: implications for the coordination environment of Fe(II) in silicate melts, *Geochim. Cosmo. Acta* 69 (2005) 4315–4332.
- [49] C.H. Booth, P.G. Allen, J.J. Bucher, N.M. Edelstein, D.K. Shuh, G.K. Marasinghe, M. Karabulut, C.S. Ray, D.E. Day, Oxygen and phosphorus coordination around iron in crystalline ferric ferrous pyrophosphate and iron-phosphate glasses with UO_2 or Na_2O , *J. Mat. Res.* 14 (1999) 2628–2639.
- [50] S. Kelly, D. Hesterberg, B. Ravel, Analysis of soils and minerals using X-ray absorption spectroscopy, in: A.L. Ulery, L.R. Drees (Eds.), *Methods of Soil Analysis Part 5: Mineralogical Methods*, Soil Science Society of America, Inc., Madison, WI, 2008, pp. 387–463.
- [51] H. Effenberger, K. Mereiter, J. Zemann, Crystal structure refinements of magnesite, calcite, rhodochrosite, siderite, smithonite, and dolomite, with the discussion of some aspects of the stereochemistry of calcite type carbonates, *Z. F. Krist.* 156 (1981) 233–243.
- [52] I.D. Brown, D. Altermatt, Bond-valence parameters obtained from a systematic analysis of the inorganic crystal structure database, *Acta Cryst.* 41 (1985) 244–247.
- [53] M. Ijjaali, G. Venturini, B. Malaman, C. Gleitzer, Synthesis, structure and physical properties of a mixed-valence iron diphosphate $\text{Fe}_3(\text{P}_2\text{O}_7)_2$: first example of trigonal prismatic Fe^{2+} with O^{2-} ligands, *Euro. J. Solid State Inorg. Chem.* 28 (1991) 983–998.
- [54] M. Karabulut, G.K. Marasinghe, C.S. Ray, G.D. Waddill, D.E. Day, Y.S. Badyal, M.L. Saboungi, S. Shastri, D. Haefner, A high energy X-ray and neutron scattering study of iron phosphate glasses containing uranium, *J. Appl. Phys.* 87 (2000) 2185–2193.
- [55] B. Ajiboye, O.O. Akinremi, A. Jurgensen, Experimental validation of quantitative XANES analysis for phosphorus speciation, *Soil Sci. Soc. Am. J.* 71 (2007) 1288–1291.
- [56] E.D. Ingall, J.A. Brandes, J.M. Diaz, M.D. de Jonge, D. Paterson, I. McNulty, W.C. Elliot, P. Northrup, Phosphorus K-edge XANES spectroscopy of mineral standards, *J. Synchrotron Rad.* 18 (2011) 189–197.
- [57] D. Hesterberg, W. Zhou, K.J. Hutchison, S. Beauchemin, D.E. Sayers, XAFS study of adsorbed and mineral forms of phosphate, *J. Synchrotron Rad.* 6 (1999) 636–638.
- [58] Z. Yin, M. Kasrai, G.M. Bancroft, K.H. Tan, X. Feng, X-ray absorption spectroscopic studies of sodium polyphosphate glasses, *Phys. Rev. B* 51 (1995) 742–750.
- [59] D. Li, G.M. Bancroft, M. Kasrai, M.E. Fleet, X.H. Feng, K.H. Tan, High-resolution Si and P K- and L-edge XANES spectra of crystalline SiP_2O_7 and amorphous $\text{SiO}_2-\text{P}_2\text{O}_5$, *Am. Mineral.* 79 (1994) 785–788.
- [60] P. Labeguerie, M. Harb, I. Baraille, M. Rerat, Structural, electronic, elastic, and piezoelectric properties of α -quartz and MXO_4 ($M = \text{Al}, \text{Ga}, \text{Fe}; X = \text{P}, \text{As}$) isomorphs compounds: a DFT study, *Phys. Rev. B* 81 (2010) 045107.